



Achieving antimicrobial and superior mechanical properties in a scalable and cost-effective heterostructured stainless steel

L. Romero-Resendiz^{a,b,1}, H.J. Kong^{c,d,1}, T. Zhang^{a,1}, H. Ni^e, S. Chen^e, M. Naeem^{f,g}, Y.T. Zhu^{a,*}

^a Department of Materials Science and Engineering, City University of Hong Kong, Kowloon, Hong Kong

^b Facultad de Química, Departamento de Ingeniería Metalúrgica, Universidad Nacional Autónoma de México, Mexico City, 04510, Mexico

^c School of Materials Science and Engineering, Dongguan University of Technology, Dongguan, 523808, China

^d Department of Mechanical Engineering, City University of Hong Kong, Hong Kong

^e Department of Infectious Diseases and Public Health, Jockey Club College of Veterinary Medicine and Life Sciences, City University of Hong Kong, Kowloon, Hong Kong

^f Department of Physics, City University of Hong Kong, Kowloon, Hong Kong

^g School of Metallurgy and Materials, University of Birmingham, Birmingham, B15 2TT, UK

ARTICLE INFO

Keywords:

Heterostructured materials
Stainless steel
Antimicrobial
Strengthening mechanisms
Mechanical properties

ABSTRACT

Heterostructured materials (HSMs) can alleviate the strength-ductility trade-off of conventional materials. Microstructure modulation by low-cost and large-scalable thermo-mechanical treatments is a feasible route to produce HSMs. Using these thermo-mechanical treatments, we have developed new heterostructured and antimicrobial stainless steels (HS&ASSs) to reduce the infection rate of multiple diseases while increasing their service life. The HS&ASSs were designed to combine several known strengthening mechanisms, which significantly improved the yield strength compared to their homogeneous counterparts while retaining good ductility. Effective antibacterial property is also observed in the HS&ASSs. The microstructural evolution and processing-microstructure-properties relationship are thoroughly explained. This work demonstrates that the improved mechanical properties of HSMs can be successfully combined with multifunctional properties, thus opening a new window for this fast-emerging field.

1. Introduction

The COVID-19 pandemic demonstrated that there is a need for new materials to deal with sanitary emergency. Microbes on fomites cause infections in patients within healthcare units [1]. Decreasing the risk of contagion by contact with contaminated surfaces is a critical issue, not only for the SARS-CoV-2 virus but also for other disease-carrying bacteria and viruses in daily life. Examples of the harmful effect of microbes are infections during intra-articular injections [2], infections in maxillofacial procedures with a mortality rate of 10–40% [3], or the near 100% occurrence of teeth damage due to microbes accumulation under molar bands and brackets of orthodontic treatments [4]. The design and development of antimicrobial materials help to overcome the potential danger of transmission of multiple microorganisms.

Stainless steel (SS) is a cost-effective material that can be combined with antimicrobial qualities for biosecurity in medical, industrial, and public sectors. However, multifunctionalities are required for some of

these applications. On the other hand, antimicrobial materials should also possess high mechanical performance to avoid the economic loss and increase safety of medical devices.

In particular, the 316L SS is extensively used in medical devices, food refrigeration components, jewelry, pharmaceutical equipment, potable water containers, wastewater treatment, marine and architectural applications, among others. However, the current properties of the 316L SS are often not enough to sustain the mechanical stress of many applications. Examples of these deficiencies include the failure of medic or orthodontic devices [5] and the breakage of hypodermic needles during clinical procedures [6,7], requiring complex and risky extraction procedures. A number of medical and daily applications need advanced mechanical performance. For example, handrails and door handles to resist continuous friction; orthodontic archwires, molar bands and brackets to withstand compression loads in the oral environment; orthodontic drills that require a high fatigue resistance, among others.

Heterostructured materials (HSMs) enable advanced mechanical

* Corresponding author.

E-mail address: y.zhu@cityu.edu.hk (Y.T. Zhu).

¹ These authors contributed equally to this work.

properties thanks to the hetero-deformation induced (HDI) strengthening [8,9]. In contrast to other materials, such as ultrafine-grained materials processed by severe plastic deformation (SPD) techniques [10], HSMs can be produced using large-scale industrial facilities at low cost [9]. The HSMs create a synergy between the mechanical response of mutually constraining soft and hard zones [11]. Due to strain partitioning, strain gradients will be generated near the soft/hard zone boundaries. To accommodate the strain gradient, geometrically necessary dislocation (GND) pile-ups will be formed in the soft zone near the interface, which produces a long-range internal stress (back stress) in the soft zone and forward stress in the hard zone [12]. The back stress and forward stress collectively produce the HDI stress [13]. The back stress strengthens the soft zones, while the forward stress makes the hard zone easier to deform. The HDI stress in HSMs becomes a new strengthening mechanism, in addition to the well-known mechanisms including grain boundaries, solid solution, twinning, dispersion of second phases, accumulation of dislocations, etc. [13,14]. Different from most of other strengthening mechanisms, the HDI strengthening can co-exist with HDI work hardening. As a result, HSMs tend to show a reduced trade-off between strength and ductility as compared to homogeneous materials [12].

From the above, the HSMs and SS have the potential to combine mechanical and antimicrobial properties for biomedical applications. Many metallic nanoparticles (NPs) with antimicrobial activity have been reported. Silver (Ag) and copper (Cu) NPs are the most widely reported against multiple microorganisms, including bacteria, viruses, fungi and algae [15]. However, Cu is much more accessible and significantly cheaper than Ag. Moreover, the latest findings pointed out a more effective antimicrobial performance of Cu than Ag [16]. Antimicrobial effectivity in homogenous Cu-bearing 316L SS has already been proven [17,18].

Improvement of mechanical properties has been reported for heterogeneous SS with Cu additions without focusing on the formation of Cu NPs [19–21]. The presence of NPs, as proposed in this work, may influence the biocidal and mechanical behaviors of the SS. A Cu-bearing heterogeneous 304 SS produced by cold rolling and annealing improved the mechanical properties compared to its coarse and cold-worked counterparts [22]. However, no aging was applied to obtain uniform distribution of Cu-NPs. Besides, the contribution of Cu-NPs to mechanical behavior, GND pile-ups-driven HDI and other strengthening mechanisms, and biocidal efficiency were not studied [22].

In this work, we aim to design a new heterostructured antimicrobial stainless steel (HS&ASS) that combines all of the so-far recognized strengthening mechanisms, i.e., solid solution (substitutional and interstitial), high density of grain boundaries, second phase dispersion, dislocation accumulation, twinning, strain-induced transformation, and HDI. This work also demonstrates the antibacterial effectiveness of the new HS&ASS. The HS&ASS of this study will serve as a basis for designing cost-effective, strong and tough, and multifunctional HSMs for the food-processing, biosafety, structural and biomedical applications.

2. Experimental procedure

2.1. Production of the HS&ASS

The raw materials were cast 316L SS and 316L SS with 3 wt% Cu additions (316LCu). The as-cast materials are referred to as initial condition (IC) hereinafter. 3 wt% Cu was selected to combine antimicrobial properties [18,23] without a large increase in stacking fault energy

(SFE) [24]. Low SFE is crucial to promote planar slip, GND pile-ups, and HDI stress [25]. The chemical composition of both alloys can be found in Table 1. 10 mm-thick plates from both alloys were subjected to a solid solution heat treatment under Ar atmosphere at 1050 °C for 30 min and posterior water quenching. Four processing routes (R1, R2, R3, and R4) were designed for a synergy between multiple strengthening mechanisms (grain boundaries density, solid solution, strain-induced phase transformation, twinning, dispersion of second phases, accumulation of dislocations, and HDI) with different grains and Cu particles size distributions. Fig. 1 shows processing parameters for the thermo-mechanical routes [26].

Microhardness and time criteria were used to select the processing parameters for solid solution (SSol), aging (A), and cold rolling (CR). Fig. 2 shows the hardness after each heat treatment and CR-processed samples. The tested heat treatment temperature and time ranges were selected based on the best mechanical behavior of heterostructured (HS) 316L SS from the literature [27]. All the heat treatments were carried out under Ar atmosphere with posterior water quenching. The CR was applied at room temperature with an average of 0.15 mm reduction per pass.

The R1 and R2 consisted of subjecting the SSol-treated condition to aging in order to precipitate Cu particles. Posterior cold rolling was applied to refine the grain size and to encourage strain-induced martensitic phase transformation. Then, a second aging (R1) or short-time annealing (STA) (R2) were applied for partial recrystallization, partial phase transformation reversion, and more Cu precipitation in the matrix. As indicated in Fig. 1, the second aging was applied at temperatures from 500 °C to 650 °C for 30–60 min. The STA was applied at 700 °C–750 °C for 5–15 min and 800 °C for 30–120 s. All heat treatments were performed at about 40 °C s⁻¹ heating rates to facilitate the combined diffusion and shear reverse phase-transformation mechanism [9].

For the R3 to R4, the SSol-treated samples were subjected to cold rolling. Posteriorly, combinations of aging (R3) and STA (R4) were applied under the abovementioned conditions. After this, the studied samples will be referred to by a three-segment identification: i) cold rolling reduction (80%) with a letter indicating previous aging (A) or only solid solution (S), ii) heat treatment temperature after CR, and iii) heat treatment holding time. For example, 80A_650_60min corresponds to a sample processed by aging, 80% thickness reduction, and heat treatment at 650 °C for 60 min (route R1), while 80S_650_60min corresponds to a sample processed by solid solution, 80% thickness reduction, and heat treatment at 650 °C for 60 min (route R3).

2.2. Microstructural characterization

The HS&ASSs were cut by water jet cutter and subjected to metallographic sample preparation to a mirror-like surface finish with colloidal silica of 0.1 μm particle size. X-ray diffraction (XRD) measurements were carried out in a D2 phaser Bruker diffractometer with LYNXEYE XE-T detector, using Cu-Kα radiation, 30 KV, 10 mA, and step size of 0.01°. For electron backscatter diffraction (EBSD), the samples were electropolished in 25 vol% HNO₃ solution at ~ -196 °C for 60 s with 20 V. EBSD analyses were carried out with a step size of 0.35 μm.

For comparison purposes, the phase contents were estimated by two methods derived from XRD and EBSD measurements. For XRD data, the direct comparison method [28] of the integrated intensity of different peaks was used. The (220), (311), and (222) peaks of the face-centered cubic (FCC) austenite phase (γ) and (200), (211), and (220) of the body-centered cubic (BCC) martensite phase (α') were used for the

Table 1
Chemical composition of the starting alloys (in wt. %).

| Alloy | C | Cr | Mn | Ni | P | Si | S | Mo | Cu | Fe |
|--------|------|-------|------|-------|------|------|------|------|------|---------|
| 316L | 0.02 | 17.03 | 1.92 | 12.04 | 0.02 | 0.72 | 0.01 | 2.56 | – | Balance |
| 316LCu | 0.02 | 17.38 | 1.91 | 12.15 | 0.02 | 0.75 | 0.01 | 2.58 | 3.01 | Balance |

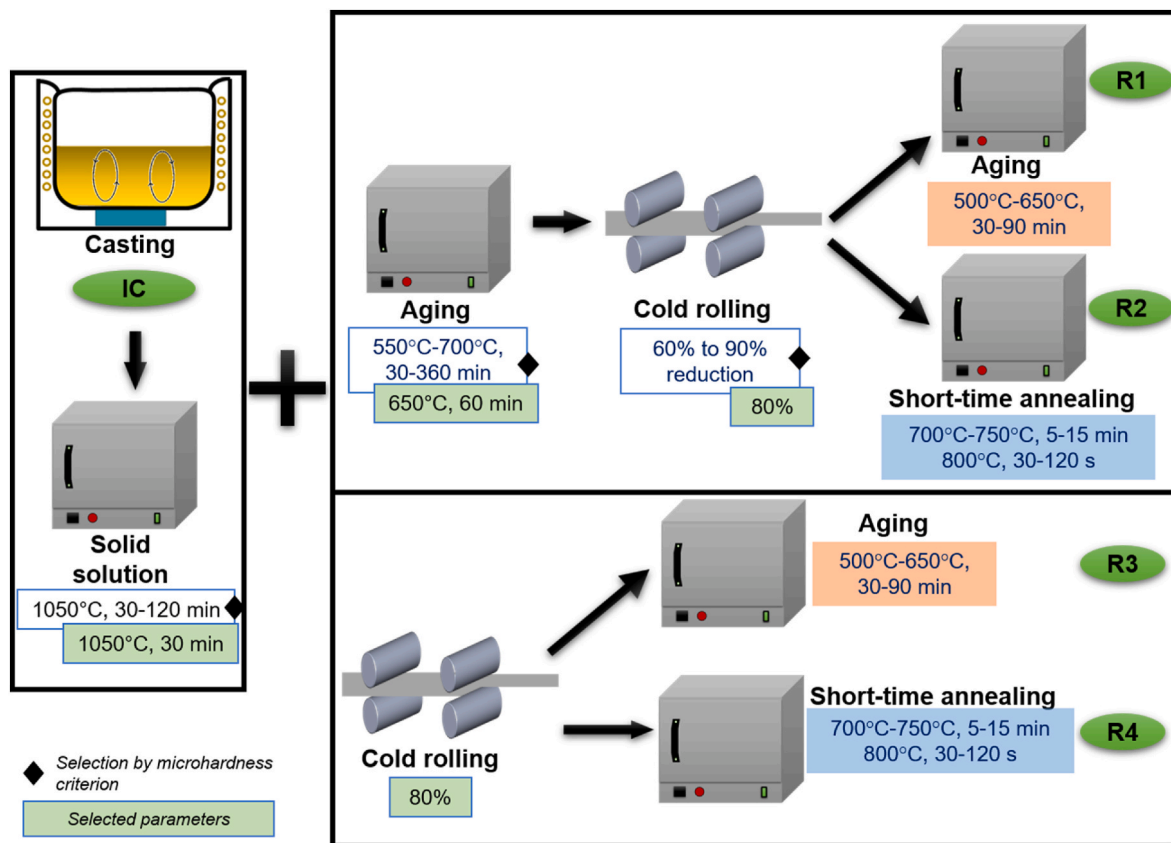


Fig. 1. The schematics of starting parameters and four thermo-mechanical routes used to elaborate HS&ASSs [26].

volume fraction estimation. From EBSD, a semi-empirical relationship between the $\gamma(220)$, $\gamma(311)$, and $\alpha'(211)$ peaks was used [29].

For transmission electron microscopy (TEM), the samples were ground up to a thickness of 50 μm and punched into 3 mm diameter discs. Electron-transparent regions were obtained in a precision ion polishing system (PIPS) Gatan 695. The observations were performed in a JEOL 2100 F TEM equipped with energy dispersive X-ray (EDX) spectroscopy at 200 keV acceleration voltage.

2.3. Mechanical behavior evaluation

Vickers hardness was measured by a BuehlerVH1202 Vickers/Knoop hardness tester with a load of 500 g and a holding time of 10 s. Hardness values were obtained by averaging at least ten indents for each sample. The HS&ASSs were cut along the rolling direction into dog-bone-shaped specimens, with a gauge length of 12.5 mm and a width-to-thickness ratio of ~ 2 . Uniaxial tensile tests were performed on Instron 3382 universal testing machine with a strain rate of 10^{-4} s^{-1} at room temperature. For each condition, three tensile samples were tested.

2.4. Antibacterial assessment

The plate counting method was used to evaluate the antibacterial effect. *E. coli* ATCC 25922 was inoculated in a sterilized TSB (CM0129, OXOID Co.) agar plate and incubated at 37 °C for 24 h. Subsequently, single colony was diluted to $\text{OD}_{600\text{nm}} 0.05$ ($\sim 10^7 \text{ CFU ml}^{-1}$) with sterilized PBS buffer ($\text{pH} \cong 7.4$, Sigma-Aldrich) using a UV-Vis spectrophotometer (DR3900, Hach Co.). The final concentration was $\sim 10^6 \text{ CFU ml}^{-1}$ with a 10-fold dilution. The materials with a surface area of 1 cm^2 ground with SiC up to 2000 grade were autoclaved before the test. Posteriorly, the materials were introduced into a 24-well plate and inoculated with 50 μl bacterial suspension solution on their surface and

incubated at 37 °C. Next, the metal sheets were picked up at different time points (0.5 h, 1 h, 2 h, 6 h, and 24 h), washed with 2450 μl PBS buffer, and resuspended with a vortex mixer (MX-S, Dragon Laboratory Instruments Ltd.) for 60 s. Finally, 100 μl of the resuspended bacterial solution was spread on the TSB agar plate and incubated for 24 h. The survival rate was calculated by Eq. (1).

$$C\% (\text{CFU ml}^{-1}) = [1 - (C_{mi} - C_t) / C_{mi}] \times 100\% \quad \text{Eq. (1)}$$

where C represents the bacterial survival rate, C_{mi} is the average bacterial concentration at the material surface at 0 h (in CFU ml^{-1}), and C_t represents the average bacterial concentration at the different testing times (in CFU ml^{-1}). Three replicates per studied condition were tested for statistical purposes.

3. Results

3.1. Microstructural assessment

From the XRD data (Fig. S1 in supplementary material), all the samples consist of FCC- γ and BCC- α' phases. Fig. 3 shows the estimation of martensite contents by EBSD and XRD measurements for the 80S series, which showed a microstructural evolution qualitatively similar to that of the 80A series. The calculation from EBSD tends to estimate higher α' contents than the XRD. However, both should be considered qualitative rather than quantitative. The EBSD method has lower statistics and may overestimate the α' due to metallographic preparation strain. The XRD method does not consider the effect of crystallographic texture, which may be relevant after rolling or recrystallization processes that tend towards Goss- and brass-like or cube-like texture in SS, respectively [9]. Despite the quantitative disparities, both methods follow similar qualitative tendencies towards decreasing α' vol% with increasing aging temperature and time.

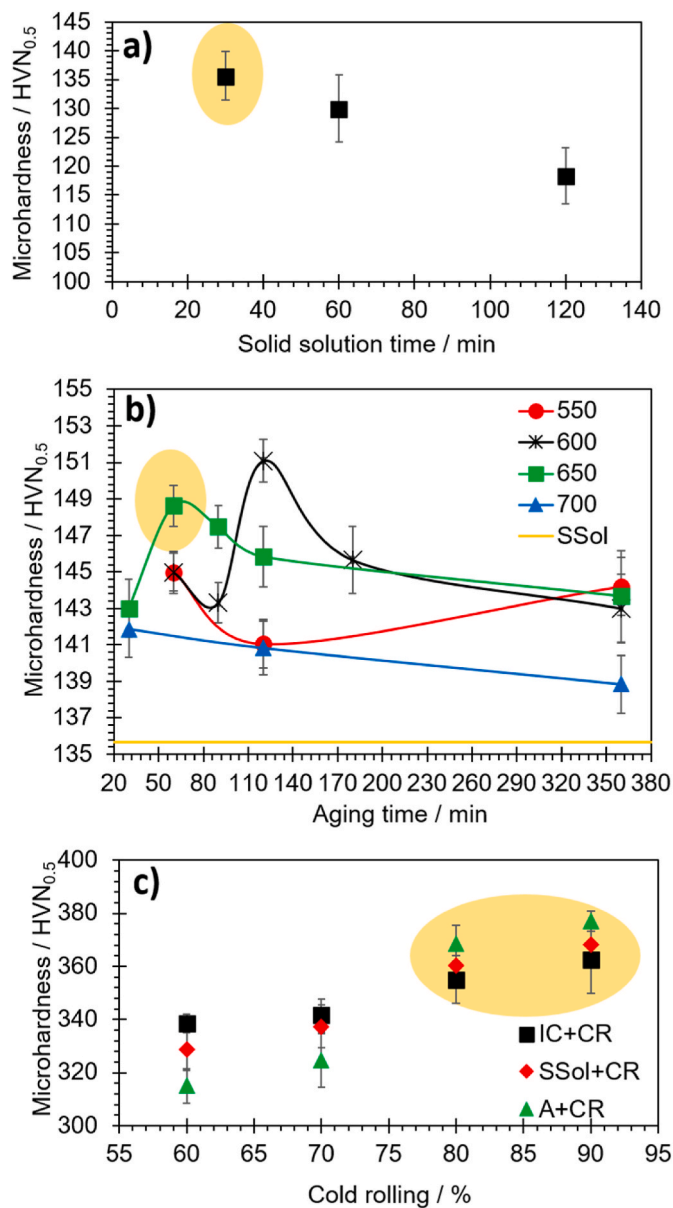


Fig. 2. Selection of processing parameters for a) solid solution (SSol) at 1050 °C, b) aging (A), and c) cold rolling (CR), which were used for performing the R1-R4 thermomechanical routes. The selected parameters are highlighted in yellow. (For interpretation of the references to color in this figure legend, the reader is referred to the Web version of this article.)

From the XRD method (Fig. 3), the IC sample comprises 89.7 vol% of γ phase and 10.3 vol% α' phase. In the SSol and SSol+80CR samples, the volume fraction of α' phase increased to 15.4% and 28.3%, respectively. The strain-induced martensite fraction is lower than the theoretically expected from the Ahmedabadi et al. [30] and Shin et al. [31] models. Considering an equivalent deformation of about 1.8 after 80% CR, the expected vol% of α' is about 80% of both models [29]. Thus, α' suppression might have occurred and will be discussed in section 4.1.

Fig. 4 shows main defects in the HS&ASS 80A and 80S samples. The HS&ASS samples showed stacking faults and nanometric grain regions (Fig. 4a and b). From the previously reported HS 316L SS [27], nano-twins are also expected in the HS&ASSs. Selected area electron diffraction (SAED) images were inserted in Fig. 4c and d to show nano-twins and nano lamellae, respectively. Besides, TEM images and EDS analyses (Fig. 4e) showed Cu precipitates, which could be expected from the low solubility of Cu in the Fe matrix [32], which can be verified

from the binary phase diagram [33]. Thus, the main observed defects by TEM in the HS&ASSs are dislocation tangles (statistically stored dislocations, SSDs), nano-twins, nano lamellae within grains, and stacking faults. These defects have been previously reported in non-antimicrobial HS 316L SS [27]. However, from the low SFE of the 316L SS, planar slip and GND pile-ups can be expected [9]. For grain morphology and GND estimations, EBSD of the representative HS&ASS 80A_650_90min, 80A_750_600s, 80S_650_90min, and 80S_750_600s samples are shown in Fig. 5. The HS&ASS samples constitute of ultrafine grains (UFG) and lamellar coarse grains (LCG), i.e., forming heterostructured lamella structure (HLS) arrangements. These HLS microstructures are similar to those reported in HS 316L [27]. Due to the difference in grain size and grain distribution, it can be observed that harder UFG zones surround softer elongated LCG zones.

The mutual constraining and high mechanical mismatch between soft and hard regions are essential for activating substantial HDI strengthening [9]. From Fig. 2, a difference of more than 100% in hardness can be expected among the fine-grained 80% CR condition (360–368 HVN_{0.5}) and coarse SSol or A conditions (135–148 HVN_{0.5}). Thus, high GND pile-up density is expected near high-mechanical mismatch interfaces, such as the ones between coarse and fine grains.

Fig. 5b.1 to 5e.1 shows the presence of GND pile-ups in green color. As expected, they are mainly formed in the soft zones (coarse grains), which experience higher deformation than the hard zones [9]. While the IC sample has 2.9×10^{12} GNDs m^{-2} , the HS&ASS 80A_650_90min (18.5×10^{12} GNDs m^{-2}), 80A_750_600s (19.1×10^{12} GNDs m^{-2}), 80S_650_90min (9.2×10^{12} GNDs m^{-2}), and 80S_750_600s (8.6×10^{12} GNDs m^{-2}) all showed higher values. The back stress results from GND pile-ups in the softer regions, while forward stress appears in the harder regions as a consequence of mutual constraining [34]. Thus, a significant contribution of HDI stress can be expected in the HS&ASSs, which may improve their mechanical behavior compared to conventional SS and previously reported antimicrobial SS. The comparison of mechanical behavior between the HS&ASS and other reported homogeneous and HS 316L will be discussed in sections 3.2 and 4.2.

3.2. Mechanical behavior evaluation

Fig. 6 shows the hardness of the reference homogeneous conditions (A, SSol, A+80CR, and SSol+80CR) and the 80A and 80S series of the HS&ASSs produced by different thermo-mechanical routes. The R1 and R3 showed the highest hardness values compared to the R2 and R4. The difference in hardness may be related to the Cu-particle dispersion during the last stage of aging. A similar increase in hardness due to Cu precipitation in 316L SS has been reported in the literature [35,36].

Fig. 7 shows the results from tensile measurements in the reference homogeneous and 80A and 80S series of the HS&ASSs samples produced by different thermo-mechanical routes. The higher UTS in the R1 and R3 processed samples agreed with their higher hardness shown in Fig. 6.

3.3. Antibacterial assessment

To probe the antibacterial efficacy of new HS&ASSs, the best mechanically performed materials (80A_650_90min, 80A_750_600s, 80S_650_90min, and 80S_750_600s) selected from section 3.2 were subjected to the plate counting method (Fig. 8). The bacterial survival rate of *E. coli* decreased more sharply and is at least 14% higher in the Cu-bearing samples (homogeneous and HS&ASS 316LCu) compared to the control sample without copper (316L). After 6 h testing, the bacterial survival rate of 65.9% for the Cu-free control sample and from 27 to 44% in the Cu-bearing samples was observed. In all cases, the survival rate reaches nearly 0% after 24 h of testing.

No significant change was observed between the homogeneous (IC) and HS Cu-bearing (HS&ASS) samples against *E. coli* survival. This result may indicate that the bacterial survival rate has a low sensitivity to the microstructural changes between the IC and the HS&ASSs samples. The

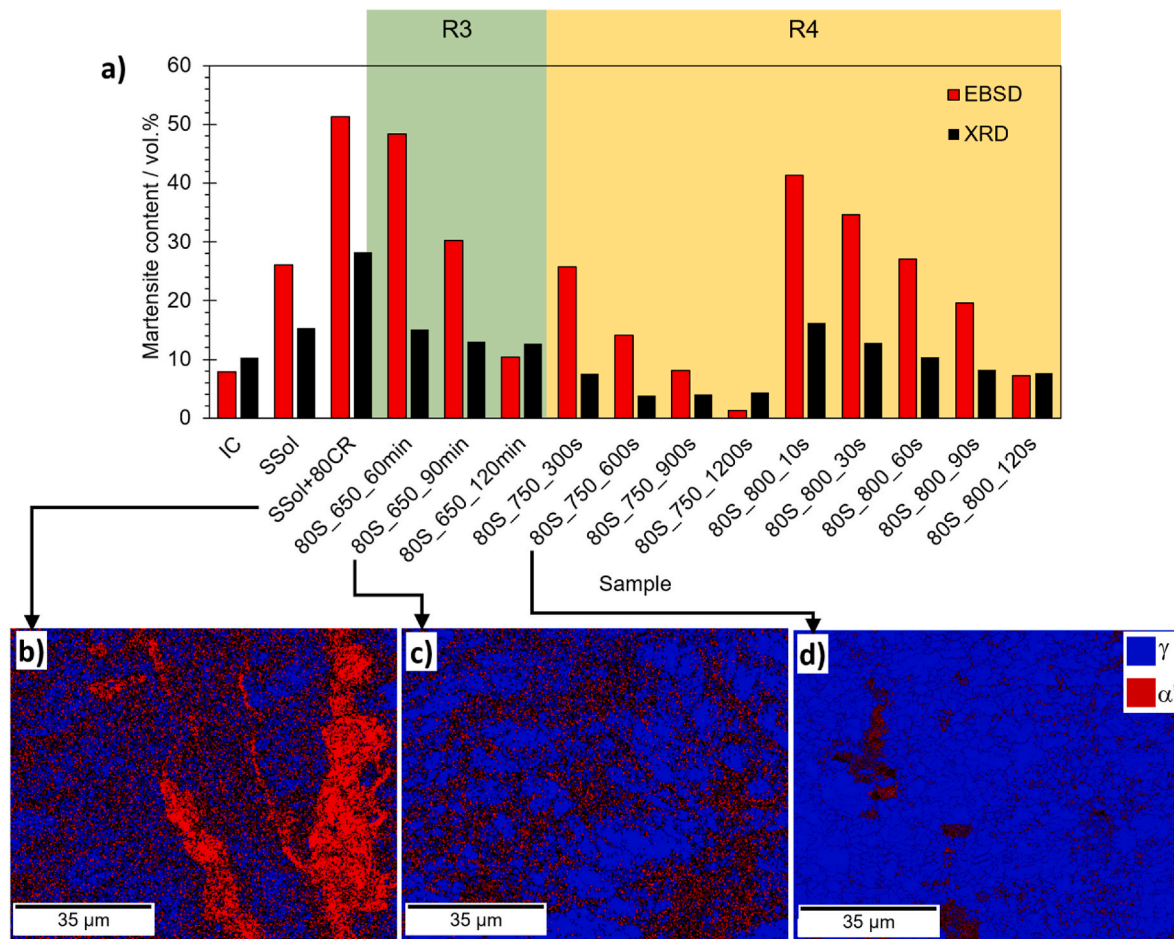


Fig. 3. Phase analysis of the 80S series of HS&ASSs produced by R3 and R4, and its comparison with homogeneous as-received (IC), solid solution (SSol), and SSol+80CR conditions. a) Phase contents of martensite are estimated by EBSD and XRD techniques, and EBSD phase contrast for b) SSol+80CR, c) 80S_650_90min, d) 80S_750_600s samples.

low bacterial rate sensitivity to the microstructure may be related to the nearly homogeneous elemental chemical distribution shown in Fig. 4. From the literature, bacterial adhesion in SS is especially sensitive to surface carbides (sensitized SS) compared to annealed and oxidized SS [37]. Regarding chemical composition distribution, the IC and the HS&ASSs are closer to the annealed conditions.

On the other hand, a higher grain boundary length of SS, such as in the HS&ASS compared to IC, is expected to increase the surface reactivity and promote ion release and cell interaction [9]. The release of Cu^{2+} from Cu-bearing 316L SS has been proven to be poisonous for bacteria [18]. However, small grain size also promotes a more compact surface oxidation layer, thus decreasing the degradation (corrosion) of the material [9]. It is possible that both mechanisms acted simultaneously in HS&ASSs. Future research on ion release, electrochemical and oxide layer formation performance on HS&ASS with different grain size distribution may be helpful to understand the low sensitivity of the *E. coli* to the microstructural arrangement.

A slight bacterial increment can be observed for the control, IC and 80S_650_90min samples. Those increments may be related to the phosphates content (Na_2HPO_4 and KH_2PO_4) in the PBS solution, which has been reported to prolong the survival of *E. coli* [38]. Other reports have also shown a slight increase in bacteria colonies, including *E. coli*, during cellular cultures in the PBS solution [39]. However, the growth tends to be low due to the near-neutral and low-nutrition nature of the PBS buffer solution.

4. Discussion

4.1. Microstructural evolution during the processing routes

From section 3.1., the samples cold rolled up to 80% reduction have a lower martensite content than theoretically expected [30,31]. The suppression of α' formation may be related to the Ni and Cr equivalents (Ni_{eq} and Cr_{eq}) as well as to the SFE of the alloy. According to the Ni_{eq} and Cr_{eq} calculated from Eq. (2) and (3) [40].

$$\begin{aligned} \% \text{ Ni equivalent } (\text{Ni}_{\text{eq}}) = & \% \text{ Ni} + \% \text{ Co} + 30(\% \text{ C}) + 25(\% \text{ N}) + 0.5(\% \text{ Mn}) \\ & + 0.3(\% \text{ Cu}) \end{aligned} \quad \text{Eq. (2)}$$

$$\begin{aligned} \% \text{ Cr equivalent } (\text{Cr}_{\text{eq}}) = & \% \text{ Cr} + 2\% \text{ Si} + 1.5(\% \text{ Mo}) + 5(\% \text{ V}) + 5.5(\% \text{ Al}) \\ & + 1.75(\% \text{ Nb}) + 1.5(\% \text{ Ti}) + 0.75(\% \text{ W}) \end{aligned} \quad \text{Eq. (3)}$$

and considering the chemical composition mentioned in Table 1, the Ni_{eq} and Cr_{eq} for 316L and 316LCu alloys are $\text{Ni}_{\text{eq} \text{ 316L}} = 13.6$, $\text{Cr}_{\text{eq} \text{ 316L}} = 22.31$, $\text{Ni}_{\text{eq} \text{ 316LCu}} = 14.608$, and $\text{Cr}_{\text{eq} \text{ 316LCu}} = 22.75$. Thus, both alloys are located at the austenite-ferrite region of the $\text{Ni}_{\text{eq}}\text{-Cr}_{\text{eq}}$ diagram (Fig. 9) [40].

From the above, both 316L and 316LCu alloys correspond to an unexpected α' region. However, BCC ferrite is linked to BCC martensite in thermodynamics calculations [41]. Besides, the expected SFE of the 316L ($\sim 64 \text{ mJ m}^{-2}$ [42,43]) is above the SFE that commonly promotes γ

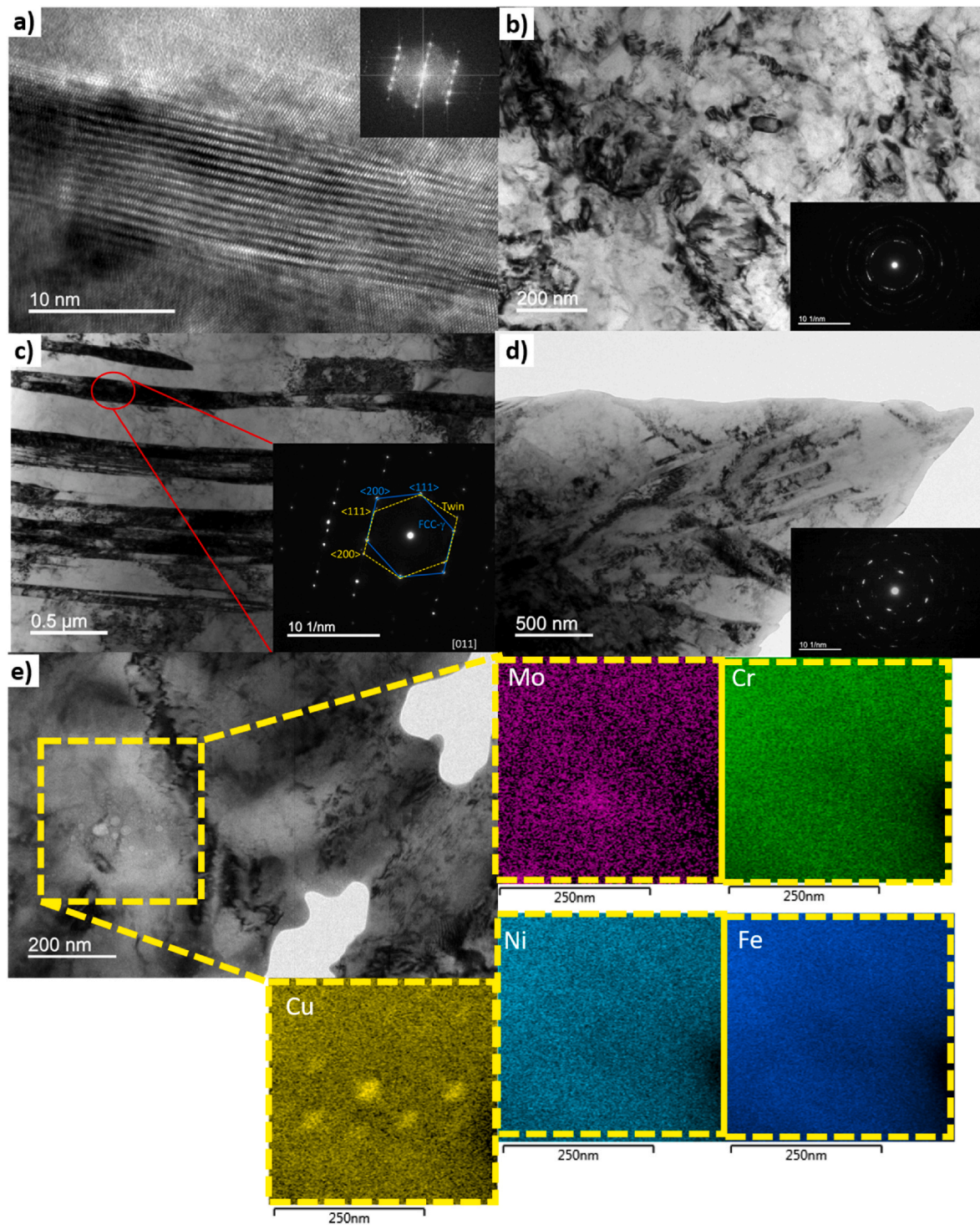


Fig. 4. Defects in HS&ASSs: a) stacking faults, b) nano-grains, c) nano-twins, and d) nano lamellae, with their respective reduced fast Fourier transform (a) or SAED (b-d) patterns, and e) Cu nanoparticles with chemical mapping by EDS.

to α' transformation (below 20 mJ m^{-2} [44]) in SS. Moreover, the Cu addition is expected to further increase the SFE of the 316L Cu alloy [24]. Due to the above, the α' phase is usually unstable in 316L SS, especially at high temperatures [27]. It has been reported a decrease from 26.4% to less than 1% of α' phase in 316L SS cold rolled and annealed at 750°C [27].

From a reported HS 316L, the increase in deformation twins, dislocations and low-angle grain boundaries is also expected from cold rolling [27]. Besides, severe grain refinement is expected as a function of the

applied strain and their mechanisms based on shear fracture and sub-division of nano-twin bundles [9,27]. To obtain the coexistence of coarse and fine grains, partial recrystallization processes were induced by consecutive heat treatments. The expected recrystallization initiation sites are the higher energy zones, i.e., fine grains instead of twin boundaries with lower energy [9].

As indicated in Fig. 1, α' to γ reversion treatments were applied after the cold rolling. The austenite finish reversion temperature has been estimated in the literature for austenitic steels with varying Cr/Ni ratios

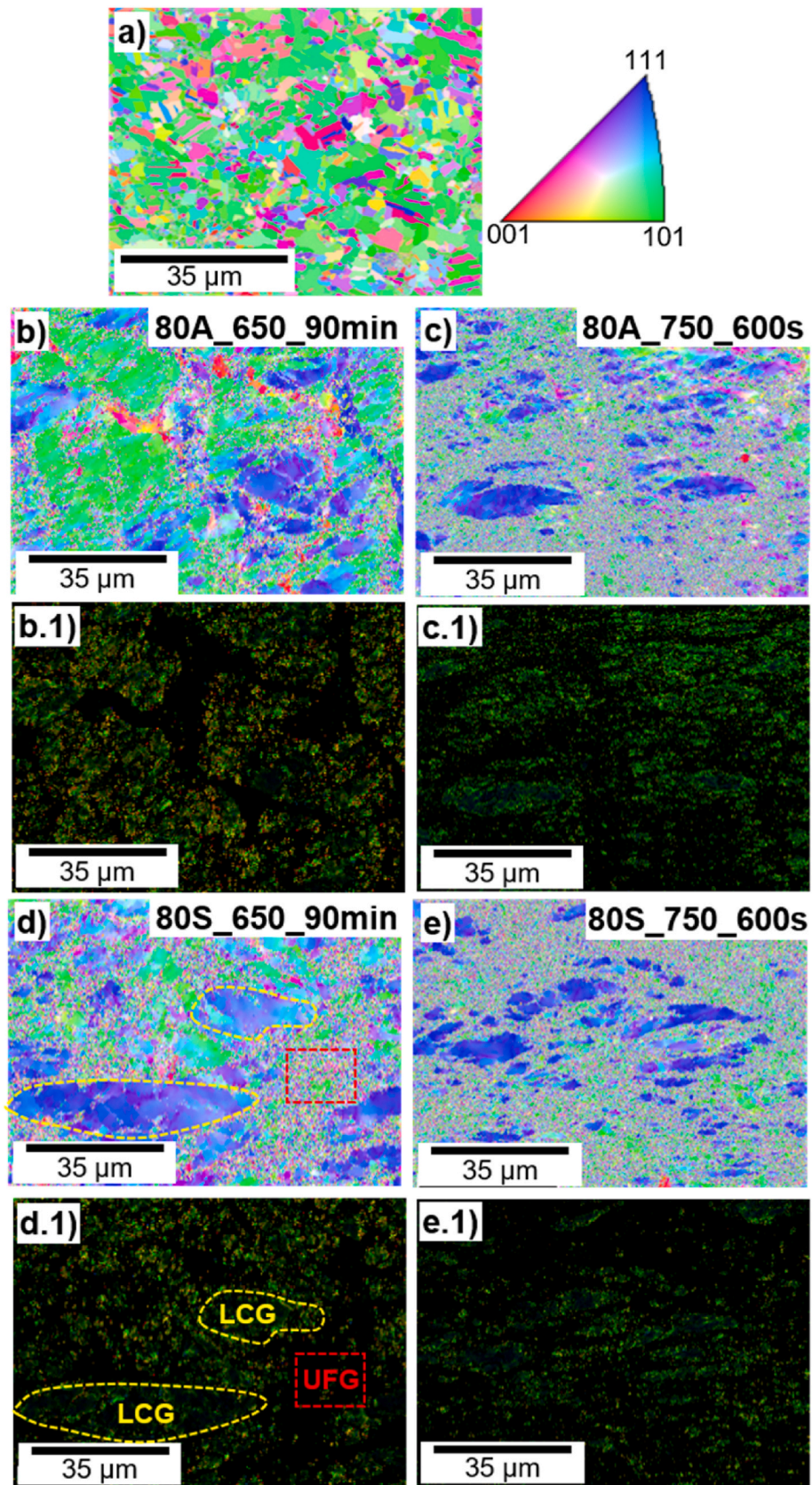


Fig. 5. EBSD micrographs that show the a-e) grains and b.1-e.1) GND pile-ups distribution in samples representative of the a) IC sample, b) 80A_650_90min (R1), c) 80A_750_600s (R2), d) 80S_650_90min (R3), and e) 80S_750_600s (R4).

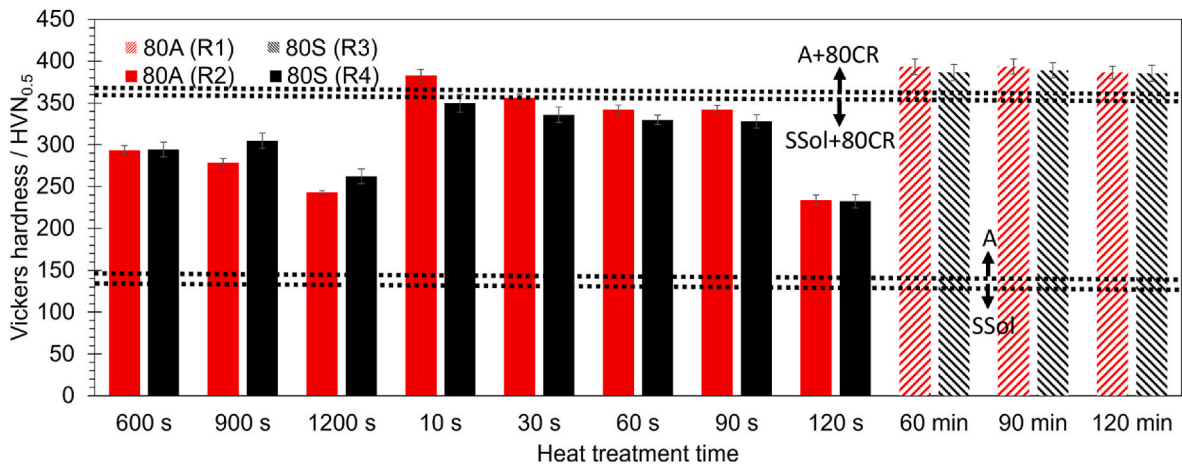


Fig. 6. Comparison of hardness obtained by the four thermo-mechanical routes (R1 to R4) in the HS&ASS and their comparison with the homogeneous coarse (A and SSol) and fine (A+80CR and SSol+80CR) conditions.

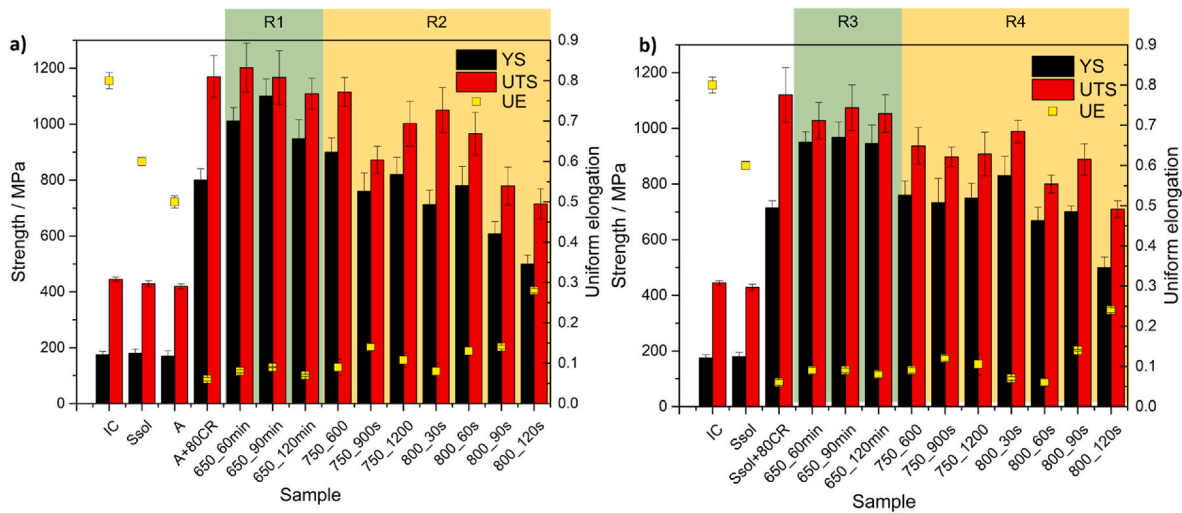


Fig. 7. Comparison of yield strength (YS), ultimate tensile strength (UTS), and uniform elongation (UE) between a) 80A and b) 80S series produced by different thermo-mechanical routes (R1 to R4).

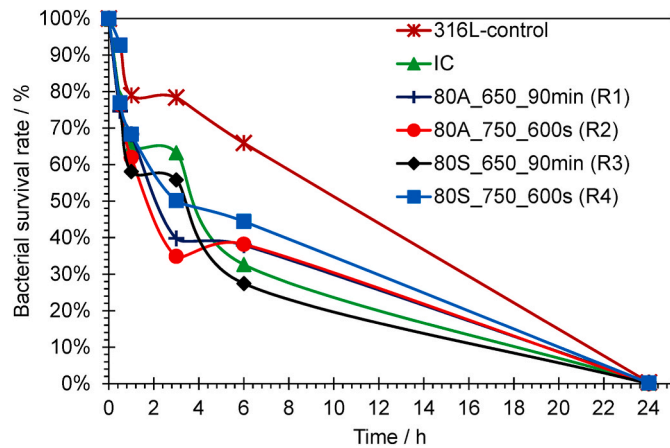


Fig. 8. Bacterial survival rate of the control sample without copper (316L) and the homogeneous (IC) and HS Cu-bearing samples produced by different thermo-mechanical routes R1-R4.

[41]. A temperature of about 625 °C should be theoretically enough for a complete reversion from strain-induced martensite to austenite. However, Fig. 3 shows the lowest α' contents by EBSD and XRD at 750 °C. The difference between the literature and the present results might be related to the effects of non-uniform grain size distribution, drag solutes (as Mo), crystallographic texture, and the effect of Cu addition that were not considered in the literature.

Because of the early recrystallization of fine grains, defects, such as nano-twins, stacking faults, dislocations (including SSDs and GNDs), and high grain boundary densities are expected. The abovementioned defects, in addition to multiphase interfaces and Cu precipitates are shown in Figs. 3 and 4. Both 80S and 80A series showed qualitatively similar microstructural evolution. The microstructure-mechanical properties relationship will be later discussed in section 4.2.

Besides the abovementioned expected defects, nano lamellae within grains were also found in the HS&ASS. The SAED inserted in Fig. 4c and d distinguish nano lamellae from nano-twins. Similar nano lamellae in shape but larger in thickness were reported in nickel produced by severe plastic deformation [45] as well as other severely cold rolled alloys [46, 47]. Lamellae are commonly formed in the rolling direction as a result of SSDs accumulation that forms dense dislocation walls after medium-level strains [46]. When increasing strain, dislocation walls arrange in dislocation cells that form new boundaries. The lamellae are

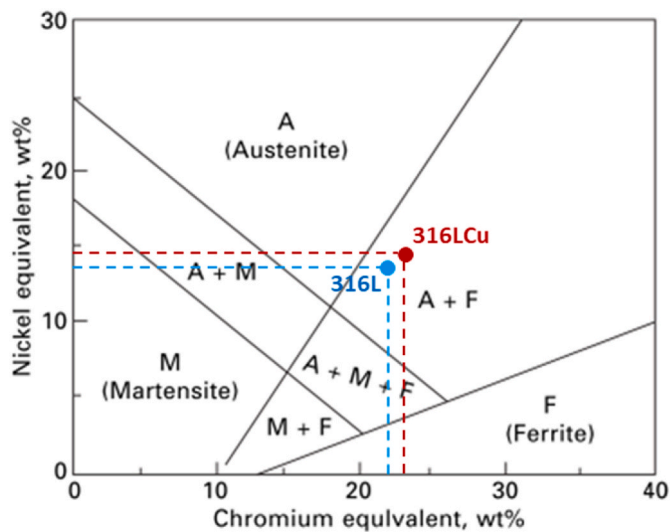


Fig. 9. Stable phase regions of the 316L and 316LCu in the Schaeffler diagram according to their specific chemical compositions after solid solution treatment at 1050 °C for 30 min and posterior water quenching. Adapted from Ref. [40].

parallel to the rolling direction and have reduced interface spacing at large strains. This phenomenon can be observed in Fig. 10a–b, where ultrafine lamellae and nano lamellae are observed in 80A and 80A_650_90 samples. Ultrafine lamellae in the 80A sample (Fig. 10a) show the presence of high density of SSDs and dislocation walls aligned to the rolling direction. It is hypothesized that the partial recrystallization heat treatments triggered the arrangement of dislocations to form new boundaries. Thus, the nano lamellae in sample 80A_650_90 (Fig. 10b) showed lower dislocation density.

Regarding the last stage of the processing routes, partial recrystallization heat treatments lead to the dislocation arrangements that form new boundaries and atomic diffusion that facilitate grain growth.

From Fig. 5, the four studied routes followed similar microstructural evolution paths at different kinetics under different temperatures. The expected microstructural evolution to form HLS SS by CR and annealing has been previously described in the literature [9,27]. The formation of shear bands and twinning are expected during CR processes in low-SFE materials, such as 316L SS [9]. Strain-induced martensite (Fig. 3) is encouraged by the presence of shear bands and twins, which acts as nucleation sites. Ultrafine grain or nanometric regions are then formed by i) shear fracture of micro-twins and γ within shear bands resulting in nano-twin and nano lamellae, and ii) dislocation accumulation at twin boundaries, generating nano-twin bundles (Fig. 4).

During annealing, the reverse transformation occurs, i.e., α' to γ phase transformation. Because of the Cr/Ni ratio of ~ 1.4 , the heating

rate of about $40\text{ }^\circ\text{C s}^{-1}$, and the high density of GND pile-ups after annealing or aging (Fig. 5), shear and diffusional reverse transformation processes may occur [9]. Only the partial recrystallization occurred due to the short time or medium temperatures used during the heat treatments.

Due to the lower energy of twin boundaries than grain or shear band boundaries [43], the reverse transformation during annealing starts at shear bands and nano-grained zones followed by the nano-twinning regions [27]. As a result, HS&ASSs composed of nano-twins, nano-grains, LCG, and recrystallized grains embedded in γ -matrix were observed in Fig. 5. From these microstructures, it is expected that the HS&ASSs combine multiple strengthening mechanisms, which will be described in the following section.

4.2. Microstructure-mechanical properties relationship

From the defects and microstructural configurations shown in section 3.1 and discussed in section 4.1., all of the known strengthening mechanisms are expected to be activated in the new HS&ASSs, i.e., interstitial solid solution, substitutional solid solution, multi-phase, TWIP, TRIP, dislocation accumulation, stacking faults, grain boundaries, second-phase dispersion (precipitates), and HDI.

Fig. 11 shows the differences in mechanical behavior between homogeneous antimicrobial [35,48], HS non-antimicrobial 316L SS [27] and the HS&ASSs. The yield strength of new HS&ASSs (up to 1100 MPa) is six times higher than that of the homogeneous 316LCu SS (175 MPa), while the ductility remains adequate for applications. The lower sacrifice of ductility with strengthening can be explained by the improvement of strain hardening rate in the HSMs obtained from the four routes. The strain hardening rate of representative heterostructured samples from R1 to R4 routes are compared with the coarse (IC) and fine (80% CR) homogeneous microstructural conditions in Fig. 12. As a general tendency for all the tested routes, the increase in heat treatment time and temperature posterior to the CR improves the hardening rate due to the formation of recrystallized grains. Those grains serve a double function as sites for dislocation accumulation, which improves strain hardening, as well as high mechanical mismatch at coarse/fine grains interfaces, which might trigger the HDI hardening. Together, strain hardening rate and stress-strain curves show the efficiency of our processing routes with the decrease in strength-to-ductility trade-off of conventional 316L in the following sequence: $R3 > R1 > R2 > R4$.

It is noteworthy that the strength-to-ductility trade-off between HS&ASS produced by R3 and the non-antimicrobial HS 316L [27] is close. As the most significant difference among them is the presence of Cu particles, it suggests that precipitates are not playing a considerable role towards strengthening. Similar results have been shown in the Cu-bearing 316L SS due to the coherent and soft nature of Cu [35,36]. Thus, Cu particles may not significantly contribute to the formation of high-mechanical mismatch interfaces. Therefore, most of the HDI stress

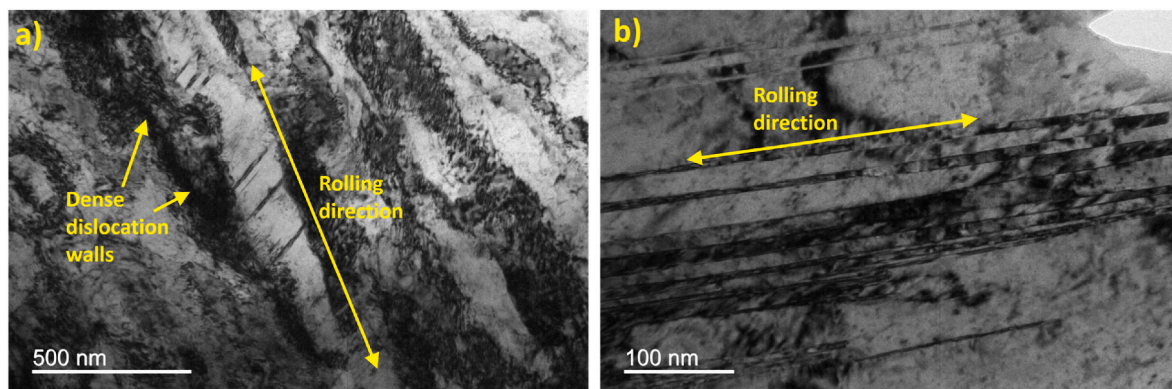


Fig. 10. Lamellae resulting from the applied strain up to 80% CR in a) 80A and b) 80A_650_90 samples.

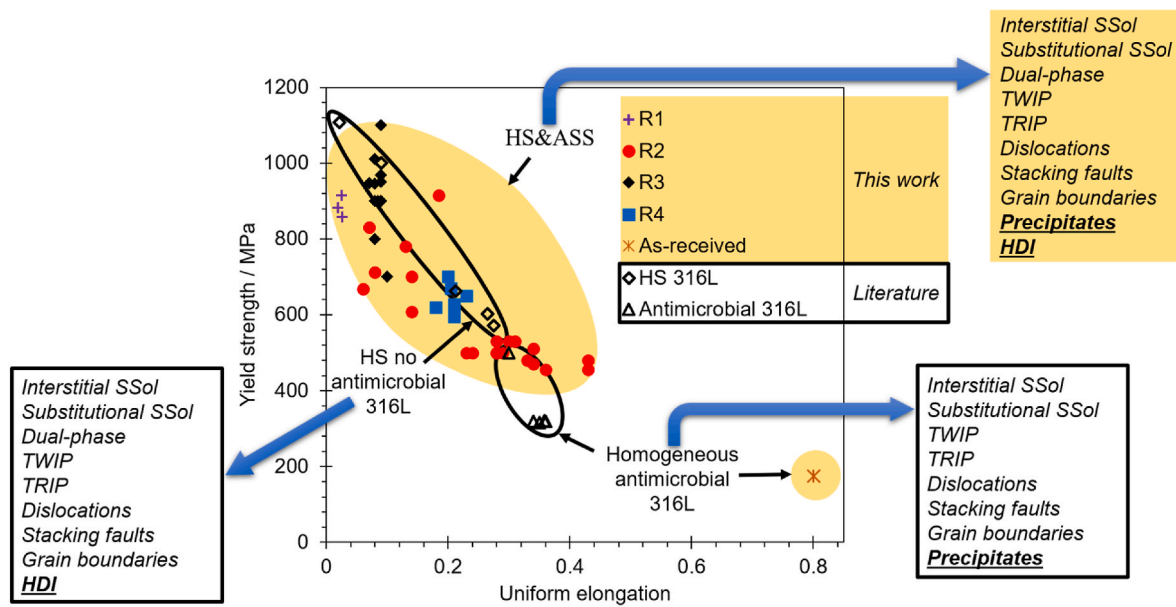


Fig. 11. Correlation between yield strength and uniform elongation of this work and results from the literature, including homogeneous antimicrobial 316L [35,48] and heterostructured antimicrobial (HS&ASS) and non-antimicrobial 316L [27]. The strengthening mechanisms associated with every class of materials are included for comparison purposes.

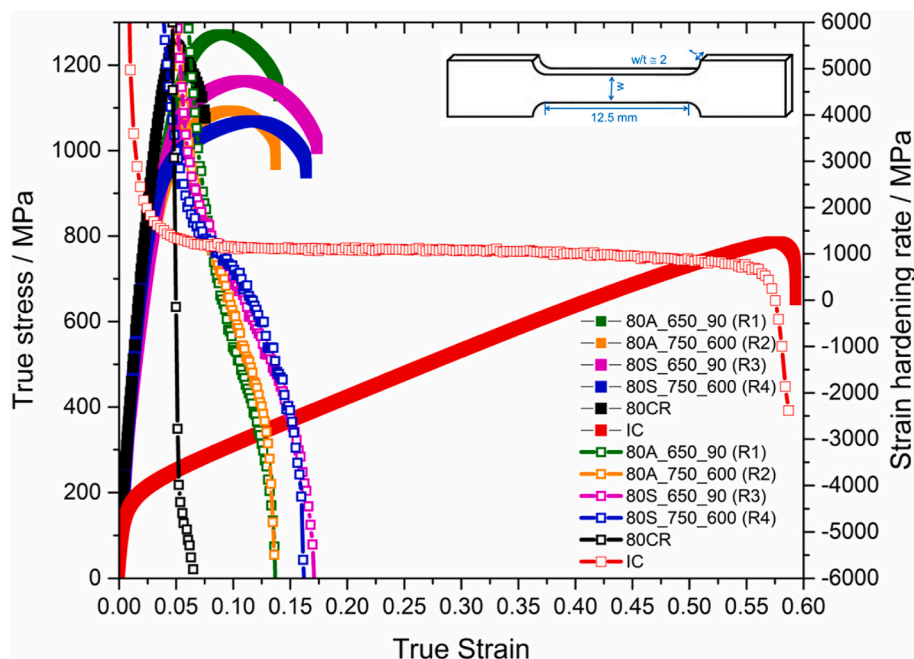


Fig. 12. Tensile stress-strain curves (solid symbols) and strain hardening rates (open symbols) of the coarse (IC) and fine (80CR) homogeneous conditions compared to the representative HS&ASSs obtained by the four different routes (R1 to R4) compared in this work.

may be caused by the mutual constraining between coarse and fine-grained regions.

5. Conclusions

Four different low-cost and scalable combinations of conventional techniques were used to produce new heterostructured and antimicrobial stainless steels (HS&ASSs). The HS&ASSs resulted in heterostructured lamella structures composed of soft lamellar coarse grains and harder ultrafine-grained zones. Multiple defects were also found in HS&ASSs, mainly interstitial and substitutional alloying elements,

twins, multiphase interfaces, statistically stored dislocations, geometrically necessary dislocations, stacking faults, nano lamellae, and copper precipitates (antimicrobial). From the abovementioned features, as well as the occurrence of strain-induced phase transformation, the HS&ASS showed an improvement of up to six times in yield strength compared to its homogeneous counterpart (1100 MPa vs. 175 MPa). An antibacterial property of the HS&ASSs was proven by killing from 55 to 72% of *E. coli* bacteria in 6 h.

This work introduces the fast-emerging field of heterostructured materials to be applied in the biomedical field and serve as a basis for future research, including systematic studies of the effect of different

antimicrobial metallic particles, the effect of crystallographic texture on the microstructural and mechanical evolutions, among others.

CRedit authorship contribution statement

L. Romero-Resendiz: Conceptualization, Methodology, Investigation, Visualization, Writing – original draft. **H.J. Kong:** Methodology, Writing – review & editing. **T. Zhang:** Methodology. **H. Ni:** Methodology, Investigation, Writing – review & editing. **S. Chen:** Investigation, Resources. **M. Naem:** Conceptualization, Validation, Writing – review & editing. **Y.T. Zhu:** Resources, Supervision, Funding acquisition, Writing – review & editing.

Declaration of competing interest

The authors declare that they have no known competing financial interests or personal relationships that could have appeared to influence the work reported in this paper.

Data availability

Data will be made available on request.

Acknowledgments

YTZ acknowledges the support from the Ministry of Science and Technology of China (2021YFA1200202), the National Natural Science Foundation of China (11988103), the Hong Kong Research Grants Council (GRF-11214121) and the Hong Kong Institute for Advanced Study of City University of Hong Kong. LRR acknowledges the funding from the Programa de Apoyo a la Investigación y el Posgrado (PAIP-50009223) of the Chemistry College of Universidad Nacional Autónoma de México. MN thanks the Asia-Oceania Neutron Scattering Association (AONSA) for the award of the AONSA Young Research Fellowship (YRF-2022).

Appendix A. Supplementary data

Supplementary data to this article can be found online at <https://doi.org/10.1016/j.msea.2023.145676>.

References

- Marquès, J.L. Domingo, Contamination of inert surfaces by SARS-CoV-2: persistence, stability and infectivity. A review, *Environ. Res.* 193 (2021) 110559–110564, <https://doi.org/10.1016/j.envres.2020.110559>.
- A.W. Chambers, K.W. Lacy, M.H.L. Liow, J.P.M. Manalo, A.A. Freiberg, Y.M. Kwon, Multiple hip intra-articular steroid injections increase risk of periprosthetic joint infection compared with single injections, *J. Arthroplasty* 32 (2017) 1980–1983, <https://doi.org/10.1016/j.arth.2017.01.030>.
- L.F. Low, H. Audimulam, H.W. Lim, K. Selvaraju, S. Balasundram, Steroids in maxillofacial space infection: a retrospective cohort study, *Open J. Stomatol.* (2021) 397–407, <https://doi.org/10.4236/ojst.2017.79034>, 07.
- A.M. Bandeira, E.F. Martinez, A.P.D. Demasi, Evaluation of toxicity and response to oxidative stress generated by orthodontic bands in human gingival fibroblasts, *Angle Orthod.* 90 (2020) 285–290, <https://doi.org/10.2319/110717-761.1>.
- J. You, S. Kim, J. Oh, H. Choi, M. Jih, Removal of a fractured needle during inferior alveolar nerve block: two case reports, *J. Dent. Anesth. Pain Med.* 17 (2017) 225–229, <https://doi.org/10.17245/jdapm.2017.17.3.225>.
- S. Seon, B. Lee, B. Choi, J. Ohe, J. Lee, J. Jung, B. Hwang, M. Kim, Y. Kwon, Removal of a suture needle: a case report, *Maxillofac. Plast. Reconstr. Surg.* 43 (2021) 1–6, <https://doi.org/10.1186/s40902-021-00309-3>.
- S. Acham, A. Truschneegg, P. Rugani, B. Kirnbauer, K.E. Reinbacher, W. Zemann, L. Kqiku, N. Jakse, Needle fracture as a complication of dental local anesthesia: recommendations for prevention and a comprehensive treatment algorithm based on literature from the past four decades, *Clin. Oral Invest.* 23 (2019) 1109–1119, <https://doi.org/10.1007/s00784-018-2525-8>.
- Y. Zhu, Introduction to heterostructured materials: a fast emerging field, *Metall. Mater. Trans. A* 52A (2021) 4715–4726, <https://doi.org/10.1007/s11661-021-06438-8>.
- L. Romero-Resendiz, M. El-Tahawy, T. Zhang, M.C. Rossi, D.M. Marulanda-Cardona, T. Yang, V. Amigo-Borras, Y. Huang, H. Mirzadeh, I.J. Beyerlein, J. C. Huang, T.G. Langdon, Y.T. Zhu, Heterostructured stainless steel: properties, current trends, and future perspectives, *Mater. Sci. Eng. R.* 150 (2022), 100691, <https://doi.org/10.1016/j.mser.2022.100691>.
- Y.T. Zhu, T.G. Langdon, The fundamentals of nanostructured materials processed by severe plastic deformation, *Jom* 56 (2004) 58–63, <https://doi.org/10.1007/s11837-004-0294-0>.
- X. Wu, Y. Zhu, Heterogeneous materials: a new class of materials with unprecedented, *Mater. Res. Lett.* 5 (2017) 527–532, <https://doi.org/10.1080/21663831.2017.1343208>.
- Y. Zhu, K. Ameyama, P.M. Anderson, I.J. Beyerlein, H. Gao, H.S. Kim, E. Lavernia, S. Mathaudhu, H. Mughrabi, R.O. Ritchie, N. Tsuji, X. Zhang, X. Wu, Heterostructured materials: superior properties from hetero-zone interaction, *Mater. Res. Lett.* 9 (2021) 1–31, <https://doi.org/10.1080/21663831.2020.1796836>.
- Y. Zhu, X. Wu, Perspective on hetero-deformation induced (HDI) hardening and back stress, *Mater. Res. Lett.* 7 (2019) 393–398, <https://doi.org/10.1080/21663831.2019.1616331>.
- X. Wu, Y. Zhu, Heterostructured Materials: Novel Materials with Unprecedented Mechanical Properties, first ed., Jenny Stanford, 2021 <https://doi.org/10.1201/9781003153078>.
- B. Khodashenas, The influential factors on antibacterial behaviour of copper and silver nanoparticles, *Indian Chem. Eng.* 58 (2016) 224–239, <https://doi.org/10.1080/00194506.2015.1026950>.
- L.T. Liu, A.W.H. Chin, P. Yu, L.L.M. Poon, M.X. Huang, Anti-pathogen stainless steel combating COVID-19, *Chem. Eng. J.* 433 (2022), 133783, <https://doi.org/10.1016/j.cej.2021.133783>.
- Y. Sun, J. Zhao, L. Liu, T. Xi, C. Yang, Q. Li, K. Yang, Passivation potential regulating corrosion resistance and antibacterial property of 316L-Cu stainless steel in different simulated body fluids, *Mater. Technol.* 36 (2021) 118–130, <https://doi.org/10.1080/10667857.2020.1734723>.
- Y. Dong, J. Li, D. Xu, G. Song, D. Liu, H. Wang, M. Saleem Khan, K. Yang, F. Wang, Investigation of microbial corrosion inhibition of Cu-bearing 316L stainless steel in the presence of acid producing bacterium *Acidithiobacillus caldus* SM-1, *J. Mater. Sci. Technol.* 64 (2021) 176–186, <https://doi.org/10.1016/j.jmst.2020.05.070>.
- H. Dong, Z.C. Li, M.C. Somani, R.D.K. Misra, The significance of phase reversion-induced nanograined/ultrafine-grained (NG/UFG) structure on the strain hardening behavior and deformation mechanism in copper-bearing antimicrobial austenitic stainless steel, *J. Mech. Behav. Biomed. Mater.* 119 (2021), 104489, <https://doi.org/10.1016/j.jmbmb.2021.104489>. Contents.
- C. Lei, X. Li, X. Deng, Z. Wang, G. Wang, Deformation mechanism and ductile fracture behavior in high strength high ductility nano/ultrafine grained Fe-17Cr-6Ni austenitic steel, *Mater. Sci. Eng. A* 709 (2018) 72–81, <https://doi.org/10.1016/j.msea.2017.10.043>.
- A. Kisko, A.S. Hamada, J. Talonen, D. Porter, L.P. Karjalainen, Effects of reversion and recrystallization on microstructure and mechanical properties of Nb-alloyed low-Ni high-Mn austenitic stainless steels, *Mater. Sci. Eng. A* 657 (2016) 359–370, <https://doi.org/10.1016/j.msea.2016.01.093>.
- M.C. Somani, M. Jaskari, S. Sadeghpour, C. Hu, R.D.K. Misra, T.T. Nyo, C. Yang, L. P. Karjalainen, Improving the yield strength of an antibacterial 304Cu austenitic stainless steel by the reversion treatment, *Mater. Sci. Eng. A* 793 (2020), 139885, <https://doi.org/10.1016/j.msea.2020.139885>.
- I.T. Hong, C.H. Koo, Antibacterial properties, corrosion resistance and mechanical properties of Cu-modified SUS 304 stainless steel, *Mater. Sci. Eng. A* 393 (2005) 213–222, <https://doi.org/10.1016/j.msea.2004.10.032>.
- A. Dumay, J.P. Chateau, S. Allain, S. Migot, O. Bouaziz, Influence of addition elements on the stacking-fault energy and mechanical properties of an austenitic Fe-Mn-C steel, *Mater. Sci. Eng. A* (2008) 483–484, <https://doi.org/10.1016/j.msea.2006.12.170>, 184–187.
- L. Romero-Resendiz, M. Naem, Y.T. Zhu, Heterostructured materials by severe plastic deformation: overview and perspectives, *Mater. Trans.* (2023), <https://doi.org/10.2320/matertrans.MT-MF2022010>. Accepted/In Press.
- L. Romero-Resendiz, Y. Zhu, T. Yang, C.-C. Huang, Patent: Heterostructured Antimicrobial Stainless Steel and Method for Synthesizing, 18/161, 2023, p. 907. Accepted/In press, <https://scholars.cityu.edu.hk/en/publications/publication/7e8a6d54-a5f0-4860-b449-548f5fcea407>.html.
- J. Li, Y. Cao, B. Gao, Y. Li, Y. Zhu, Superior strength and ductility of 316L stainless steel with heterogeneous lamella structure, *J. Mater. Sci.* 53 (2018) 10442–10456, <https://doi.org/10.1007/s10853-018-2322-4>.
- B.D. Cullity, Elements of X-Ray Diffraction, Addison-Wesley Metallurgy series, Massachusetts, 1956.
- M.J. Sohrabi, M. Naghizadeh, H. Mirzadeh, Deformation-induced martensite in austenitic stainless steels: a review, *Arch. Civ. Mech. Eng.* 20 (2020) 1–24, <https://doi.org/10.1007/s43452-020-00130-1>.
- P.M. Ahmedabadi, V. Kain, A. Agrawal, Modelling kinetics of strain-induced martensite transformation during plastic deformation of austenitic stainless steel, *Mater. Des.* 109 (2016) 466–475, <https://doi.org/10.1016/j.matdes.2016.07.106>.
- H.C. Shin, T.K. Ha, Y.W. Chang, Kinetics of deformation induced martensitic transformation in a 304 stainless steel, *Scr. Mater.* 45 (2001) 823–829, [https://doi.org/10.1016/S1359-6462\(01\)01101-0](https://doi.org/10.1016/S1359-6462(01)01101-0).
- M. Perez, F. Perrard, V. Massardier, A. Deschamps, Low temperature solubility of copper in iron : experimental study using thermoelectric power , small angle X-ray scattering and tomographic atom probe, *Philos. Mag.* 85 (2005) 2197–2210, <https://doi.org/10.1080/14786430500079645>.
- The Materials Information Society, ASM Handbook - Alloy Phase Diagrams, 1992.
- X. Wu Yuntian Zhu, Heterostructured materials, *Prog. Mater. Sci.* 131 (2023), 101019, <https://doi.org/10.1016/j.pmatsci.2022.101019>.

- [35] T. Xi, M. Babar Shahzad, D. Xu, J. Zhao, C. Yang, M. Qi, K. Yang, Copper precipitation behavior and mechanical properties of Cu-bearing 316L austenitic stainless steel: a comprehensive cross-correlation study, *Mater. Sci. Eng. A*. 675 (2016) 243–252, <https://doi.org/10.1016/j.msea.2016.08.058>.
- [36] T. Xi, M.B. Shahzad, D. Xu, Z. Sun, J. Zhao, C. Yang, M. Qi, K. Yang, Effect of copper addition on mechanical properties, corrosion resistance and antibacterial property of 316L stainless steel, *Mater. Sci. Eng. C* 71 (2017) 1079–1085, <https://doi.org/10.1016/j.msec.2016.11.022>.
- [37] R.P. George, P. Muraleedharan, K.R. Sreekumari, H.S. Khatak, Influence of surface characteristics and microstructure on adhesion of bacterial cells onto a type 304 stainless steel, *Biofouling* 19 (2003) 1–8, <https://doi.org/10.1080/08927010290031017>.
- [38] T. Juhna, D. Birzniece, J. Rubulis, Effect of phosphorus on survival of *Escherichia coli* in drinking water biofilms, *Appl. Environ. Microbiol.* 73 (2007) 3755–3758, <https://doi.org/10.1128/AEM.00313-07>.
- [39] C.H. Liao, L.M. Shollenberger, Survivability and long-term preservation of bacteria in water and in phosphate-buffered saline, *Lett. Appl. Microbiol.* 37 (2003) 45–50, <https://doi.org/10.1046/j.1472-765X.2003.01345.x>.
- [40] V. Kain, *Stress Corrosion Cracking (SCC) in Stainless Steels*, Woodhead Publishing Limited, 2011, <https://doi.org/10.1533/9780857093769.3.199>.
- [41] M.J. Sohrabi, H. Mirzadeh, C. Dehghanian, Thermodynamics basis of saturation of martensite content during reversion annealing of cold rolled metastable austenitic steel, *Vacuum* 174 (2020), 109220, <https://doi.org/10.1016/j.vacuum.2020.109220>.
- [42] B. Ravi Kumar, B. Mahato, N.R. Bandyopadhyay, D.K. Bhattacharya, Comparison of rolling texture in low and medium stacking fault energy austenitic stainless steels, *Mater. Sci. Eng. A*. 394 (2005) 296–301, <https://doi.org/10.1016/j.msea.2004.11.057>.
- [43] C. Donadille, R. Valle, P. Dervin, R. Penelle, Development of texture and microstructure during cold-rolling and annealing of FCC alloys: example of an austenitic stainless steel, *Acta Metall.* 37 (1989) 1547–1571, [https://doi.org/10.1016/0001-6160\(89\)90123-5](https://doi.org/10.1016/0001-6160(89)90123-5).
- [44] J. Lu, L. Hultman, E. Holmström, K.H. Antonsson, M. Grehk, W. Li, L. Vitos, A. Golpayegani, Stacking fault energies in austenitic stainless steels, *Acta Mater.* 111 (2016) 39–46, <https://doi.org/10.1016/j.actamat.2016.03.042>.
- [45] H.W. Zhang, X. Huang, N. Hansen, Evolution of microstructural parameters and flow stresses toward limits in nickel deformed to ultra-high strains, *Acta Mater.* 56 (2008) 5451–5465, <https://doi.org/10.1016/j.actamat.2008.07.040>.
- [46] D.A. Hughes, N. Hansen, Microstructure and strength of nickel at large strains, *Acta Mater.* 48 (2000) 2985–3004, [https://doi.org/10.1016/S1359-6454\(00\)00082-3](https://doi.org/10.1016/S1359-6454(00)00082-3).
- [47] B.L. Li, A. Godfrey, Q.C. Meng, Q. Liu, N. Hansen, Microstructural evolution of IF-steel during cold rolling, *Acta Mater.* 52 (2004) 1069–1081, <https://doi.org/10.1016/j.actamat.2003.10.040>.
- [48] L.T. Liu, Y.Z. Li, K.P. Yu, M.Y. Zhu, H. Jiang, P. Yu, M.X. Huang, A novel stainless steel with intensive silver nanoparticles showing superior antibacterial property, *Mater. Res. Lett.* 9 (2021) 270–277, <https://doi.org/10.1080/21663831.2021.1894613>.